scientific reports

Check for updates

OPEN

Construction and characterization of nano-oval $BaTi_{0.7}Fe_{0.3}O_3$@$NiFe_2O_4$ nanocomposites as an effective platform for the determination of H_2O_2

Ali B. Abou Hammad[1], Hend S. Magar[2], A. M. Mansour[1], Rabeay Y. A. Hassan[3] & Amany M. El Nahrawy[1]✉

Talented di-phase ferrite/ferroelectric $BaTi_{0.7}Fe_{0.3}O_3$@$NiFe_2O_4$ (BFT@NFO) in oval nano-morphology was chemically synthesized using controlled sol–gel processes and calcined at 600 °C. The effects of shielding using $NiFe_2O_4$ (NFO) nanoparticles on the microstructure, phase transition, thermal, and relative permittivity of $BaTi_{0.7}Fe_{0.3}O_3$ (BTF) nano-perovskite were systematically explored. X-ray diffraction patterns and Full-Prof software exhibited the forming of the $BaTi_2Fe_4O_{11}$ hexagonal phase. TEM and SEM images demonstrated that the coating of $BaTi0.7Fe_{0.3}O_3$ has been successfully controlled with exquisite nano-oval $NiFe_2O_4$ shapes. The NFO shielding can significantly promote the thermal stability and the relative permittivity of BFT@NFO pero-magnetic nanocomposites and lowers the Curie temperature. Thermogravimetric and optical analysis were used to test the thermal stability and estimate the effective optical parameters. Magnetic studies showed a decrease in saturation magnetization of $NiFe_2O_4$ NPs compared to their bulk system, which is attributed to surface spin disorder. Herein, characterization and the sensitive electrochemical sensor were constructed for the evaluation of peroxide oxidation detection using the chemically adjusted nano-ovals barium titanate-iron@nickel ferrite nanocomposites. Finally, The BFT@NFO exhibited excellent electrochemical properties which can be ascribed to this compound possessing two electrochemical active components and/or the nano-ovals structure of the particles which can further improve the electrochemistry through the possible oxidation states and the synergistic effect. The result advocates that when the BTF is shielded with NFO nanoparticles the thermal, dielectric, and electrochemical properties of nano-oval $BaTi_{0.7}Fe_{0.3}O_3$@$NiFe_2O_4$ nanocomposites can be synchronously developed. Thus, the production of ultrasensitive electrochemical nano-systems for the determination of hydrogen peroxide is of extensive significance.

In recent years, perovskite materials have been well studied. The most prominent ABO_3 ferroelectric materials have attracted considerable attention as catalysts due to their geometric and electronic stability, higher dissolution resistance in aqueous and non-aqueous solutions, and cost-efficiency. There is rare existence of crystalline multiferroic compounds in which ferromagnetism and ferroelectricity coexist at room temperature[1]. Due to their potential application in the developing field of information storage, spintronics, and multiple-state memory storage devices, such compounds are currently under intensive study[2,3]. Enormous attempts were made to improve the room temperature ferromagnetism and ferroelectricity in perovskite ceramics. Various approaches are underway to explore the possibility of synthesizing materials with superior multiferroic efficiency. Another possible method of magnetic doping is of TM (transition metal) ions (Fe^{3+}, Co^{2+}, Ni^{2+}, Mn^{2+}, etc.) through ferroelectric materials[4,5].

[1]Solid State Physics Department, Physics Research Division, National Research Centre, 33 El Bohouth St., Dokki, Giza 12622, Egypt. [2]Applied Organic Chemistry Department, National Research Centre (NRC), 33 El-Bohouth St., Dokki, Cairo 12622, Egypt. [3]Biosensors Research Laboratory, Zewail City of Science and Technology, 6Th October City, Giza 12578, Egypt. ✉email: amany_physics_1980@yahoo.com; am.elnahrawy@nrc.sci.eg

A major class of ferroelectric material that shows a piezoelectric effect and a high dielectric permittivity for technological applications, such as transducers, surface acoustic waves (SAW), and ferroelectric random-access memories (FeRAM) devices[6]. In the composition of perovskite ABO_3, both cations (A and B), whereas the A atoms are greater than the B atoms. The ionic radii of Fe^{3+} (0.645 Å) are larger than Ti^{4+} (0.605 Å), whereas Ba^{2+} has larger ionic radii (1.35 Å). BTO has a general ABO_3 configuration in which Ba^{2+} and O^{2-} ions create a close-packed cubic lattice with Ti^{4+} ions occupying the oxygen (O^{2-}) generated octahedral holes. The $BaTiO_3$ structure has a three-dimensional array of TiO_6 corners sharing octahedral with Ba^{2+} ions in the 12-fold cavities between the polyhedra. The arrangement of the atoms is known as the close-packed array of the A^{2+} and O^{2-} ions together[7]. In addition to its structure and size, the properties of BTO depend on its chemical composition. Doping with equivalent elements, perovskite material shows interesting electrical characteristics for the $BaTiO_3$ based on the chemical states of the components and the surface chemistry of the specimens. However, the major phenomenon of these nanomaterials is the partial substitution of the cations at the A and B sites of ABO_3 as well as their ability to preserve the stability in the crystal structure of uncommon mixed oxidation states[8,9]. An interesting aspect of Ba, Ti, Fe, and O ions in bulk materials has been discussed concerning both electronic deficiency and surface toxicity. Several recent studies have been addressed based on photoelectron spectroscopy for the chemical analysis (ESCA) of calcined $BaTiO_3$ nanomaterial doped with Fe^{3+} ions[9–12]. ESCA or XPS is a surface morphological technique that can be used to obtain information on the chemical state or valence state and the electronic information at the core level for the constituent element[9–12]. Pure $BaTiO_3$ has lower ionic conductivity and acts as an insulator at room temperature. The defect model indicates that the substitution of the Ti-site by the acceptor impurities is the reason for the formation of charge carrier and oxygen vacancies that increase both the ionic and electronic conductivity. The dominant charge carrier depends on the synthesis conditions and the amount of unintentional impurities of the acceptor and the donor. In $BaTiO_3$ ceramics, Fe^{3+} ions usually replace Ti^{4+}, where Fe^{3+} ions are considered to have a 3 + valence. Therefore oxygen vacancy should be created to preserve the charge neutrality of the perovskite structure ($BaTi_{1-x}Fe_xO_{3-\delta}$, δ-oxygen vacancy). Abdel Aal et al. 2014 successfully prepared $BaTi_{1-x}Fe_xO_3$ by sol–gel, where the trivalent ions (Fe^{3+}) replace the tetravalent ions Ti^{4+} and create oxygen vacancy to maintain the charge neutrality of the compound[13].

Understanding the impact of the substitution of TM on structural, physical, and microstructural properties will be a significant step in the explanation of these properties[14–16]. Nickel ferrite, as an inverse spinel-type with molecular form ($NiFe_2O_4$), offers ferrimagnetism behavior that originates from trivalent (Fe^{3+}) and the divalent (Ni^{2+}) cations distribution in B and A locations. In the $NiFe_2O_4$ structure, (Ni^{2+}) ions are in B-sites, and trivalent (Fe^{3+}) ions are equally divided between both (A and B) sites[17]. $NiFe_2O_4$ nanoparticles are used in various applications because of their extraordinary properties including lower toxicity, small magnetic anisotropy, excellent electrochemical activity, elevated electrical conductivity, and lower Curie temperature. Usually, their properties are constructed on synthesis manner, size scale, and the grain shape of the $NiFe_2O_4$ material[18–20].

Abou Hammad et al. 2020 have prepared Perovskite/spinel nanocomposites by advanced sol–gel, where they prepared the spinel ferrite $CoFe_2O_4$ powders then they coated it by $ZnTiO_3$ through dispersing the $CoFe_2O_4$ nanopowders in $ZnTiO_3$ solutions and drying the solution with slow rate to enable building up the shell layer ($ZnTiO_3$)[21].

On the other hand, the development of reliable and sensitive sensors for hydrogen peroxide detection by an easy method using a low-cost way is important. Many analytical techniques have been carried out for H_2O_2 detection, such as chemiluminescence[22], fluorescence[23], spectrophotometry, chromatography, and electrochemistry[24–27]. Electrochemical detection is distinctive due to simplicity, selectivity, sensitivity, and low cost[28–34]. The electrochemical biosensor is an ideal detection tool for the fast, sensitive, and accurate detection of drugs[35], biological samples, and the diagnosis of diseases[36]. All of these interesting properties of the electrochemical sensors depend on the type of electrode materials. Hence, it is necessary to provide new nanomaterials that have electro-catalytic properties to evaluate an effective electrochemical sensor platform(s). When controlled the energy band of BTO-nanostructures, the optoelectronic and catalytic activity will be developed to meet the advanced applications.

Therefore, in this work, the piezoelectric BTO shielded with ferrites will acquire a partial semiconducting property hybridized with efficient electric, catalysts, and electrochemical performance can lead to significantly enhanced catalysis operation according to the piezo-nanomagnetic catalysis effect.

Hence, the study of spinel ferrites as a shield layer for the perovskite is considered of scientific and industrial enormous importance because of their new properties, significant magnetic and electrical properties, excellent chemical stability, and wider applications. The present study investigates the impact of doping of NFO NPs with various concentrations on BTF nanoperovskite. Also, the ability of nano-oval $BaTi_{0.7}Fe_{0.3}O_3$@$NiFe_2O_4$ nanocomposites as an effective platform for the determination of H_2O_2 is investigated. The structural, thermal, optical, dielectric, and electrochemical properties of the nanomaterials have been studied. Due to the high electrocatalytic activity properties of doping of $NiFe_2O_4$ ions with various concentrations on the BTF materials, there are modifications on the screen-printed electrodes surface, and the direct electrochemical oxidation of peroxide was studied using cyclic voltammetry and chronoamperometric techniques. The prepared nanostructures showed high sensitivity toward peroxide detection, which can be effective in the enzymatic biosensor fields.

Materials and methods

Materials. For the synthesis of Ba $Fe_{0.3}Ti_{0.7}O_3$and $NiFe_2O_4$phases, high grade titanium (IV) isopropoxide $Ti[OCH(CH_3)_2$, barium acetate ($Ba(CH_3COO)_2$,99.9%), iron nitrate $Fe(NO_3)_3$. $9H_2O$ (99.9%),$Ni(NO_3)_2.6H_2O$ (98%), acetyl acetone (AcAc, $C_5H_8O_2$, and nitric acid(HNO_3) were used as a raw materials. Potassium ferrocyanide, potassium ferricyanide, potassium chloride, potassium dihydrogen phosphate, potassium monohydrogen

phosphate, hydrochloric acid (HCl), sodium hydroxide (NaOH), and hydrogen peroxide were purchased from Sigma-Aldrich.

Synthesis of multiferroic $BaTi_{0.7}Fe_{0.3}O_3$ shielded with $NiFe_2O_4$ nanocomposites. First, in the $NiFe_2O_4$ coating layer, the stoichiometric amounts of $Fe(NO_3)_3{\cdot}9H_2O/H_2O$ and $Ni(NO_3)_2{\cdot}6H_2O/H_2O$ are mixed in (1:2) ratio with a dissolved citrate acid (CA) under stirring. After hard stirring for 1 h, the NFO sols aged at room temperature (RT) for 5 h before coating BTF nanocrystallites.

Iron barium titanate (BTF) shielded with nickel ferrite ($NiFe_2O_4$, NF) was synthesized by the adapted sol–gel process. The sol–gel process allows the formation of multiferroic magnetoelectric and the controlled coexisting of magnetic and electric phases in one structure.

Barium titanate iron nanocrystallites were prepared by sol–gel process using the evaluated amounts of barium acetate, titanium (IV) isopropoxide, and iron nitrate as a source of Ba, Ti, and Fe, respectively. Acetic acid (HAc) and acetylacetone (AcAc, $C_5H_8O_2$) were used as suitable solvents. Titanium (IV) isopropoxide was dissolved in acetylacetone, while both barium acetate and iron nitrate were dissolved in acetic acid/water. The solutions were mixed, stirred for 1.30 min, and dried at 200 °C. Further, thermal treatment was done at 450 °C for 2 h, after which barium titanate iron powder was shaped (Fig. 1).

For BTF/(x) NF (x = 0, 1, 3, and 5), the resulting BTF nanopowder, after calcination at 450 °C, was added to the solution of $NiFe_2O_4$ according to the desired weight percent. The obtained solution was stirred for 1 h at 80 °C. The solution dried at 200 °C and turned into a viscous brawn gel, and started yielding xerogel form after evaporating the aqueous media. Finally, the obtained xerogels were calcinated at 600 °C. The constructed nanocomposite samples were labeled with symbols 0B, 1B, 2B, and 3B.

Material characterizations. The prepared perovskite-$NiFe_2O_4$ nanocomposites were characterized using the powder X-ray Diffraction (XRD-XPERT) through (Cu Kα) radiation. The profiles of XRD for the nano-oval $BaTi_{0.7}Fe_{0.3}O_3$@$NiFe_2O_4$ nanocomposites were then refined using fixing the instrumental and shape parameters by Full-prof software (the Pseudo-Voigt fitting-model) and geometrical assembly was drawn by the VESTA: win64 software[37,38]. Transmission electron microscopy (High-resolution-TEM, (FEI; Tecnai- T20)) was used.

Thermogravimetric analysis measurements (TGA) in flowing imitation air (flow rate 20 ml/min, heating rate 50 K/min) of the pre-dried 200 °C solutions was achieved using Netzsch (STA 449 system), with a heating rate of (10 °C/min).

The optical bandgap of the nano-oval composites was evaluated using UV–Vis-diffuse reflectance spectroscopy (JASCO: V550) and also the optical bandgap can be evaluated through Tauc Plot manner.

Dielectric capacities were achieved using (LCR METER-IM3536) by a frequency range of 4 Hz–8 MHz. The samples were pressed in a distinct die (diameter = 10 mm) to procedure tablets with a thickness of ~ 1.2 mm.

Electrochemical analyses. Screen printed electrodes (SPEs) were used as the sensing platform for testing the electrochemical properties of the newly synthesized nanocomposites. Electrochemical techniques (cyclic voltammetry (CV), and electrochemical impedance spectroscopy (EIS)) were conducted using CHI-potentiostat. For electrode surface modification with the nanomaterials, 5.0 mg of the synthetic nanocomposite was added to 1.0 ml double distilled water and then ultra-sonicated for up to 30 min to produce a homogenous

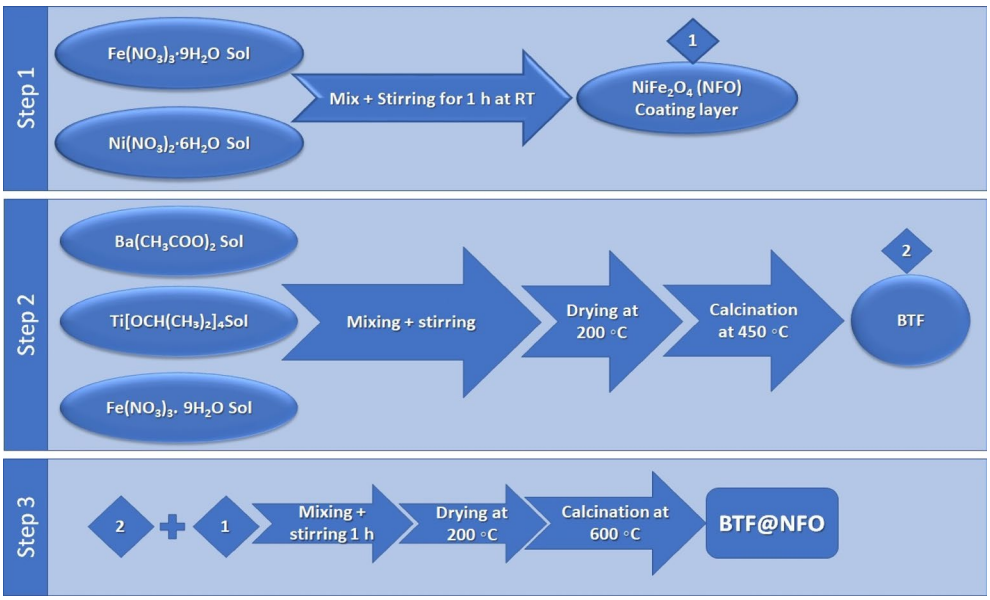

Figure 1. Synthesis steps of multiferroic BaTi0.7Fe0.3O3 shielded with $NiFe_2O_4$ nanocomposites.

suspension. Then 30 µl of the suspended solution was dropped on the SPE surface and left to dry. For SPE characterization, CV and EIS measurements were carried out in a solution containing 5 mM of the ferricyanide [Fe $(CN)_6]^{3-/4-}$ and 0.1 M KCl. For H_2O_2 detection chronoamperometric measurements were carried out in a PBS buffer. The following figure (Fig. 2) shows the simple modification method of SPEs with the 0B, 1B, 2B, and 3B nanocomposites for testing their electrochemical performance[34].

Results and discussion

phase identification (XRD). The formation of nano-oval $BaTi_{0.7}Fe_{0.3}O_3$ shielded (1, 3, 5 mol.%) $NiFe_2O_4$ nanocomposites are confirmed by the XRD profile/ FullProf as revealed in Fig. 3a–d. Obviously, the growth of hexagonal $BaTi_2Fe_4O_{11}$ and cubic $NiFe_2O_4$ phases indicated that the lower calcination core BTF nanoparticles had been reacted with the shield $NiFe_2O_4$ for new arrangement within the $BaTi_{0.7}Fe_{0.3}O_3$@ $NiFe_2O_4$ complex. Figure 3a, d show a presence of a secondary phase (monoclinic phase of $Ba_3Fe_{10.168}Ti_{0.832}O_{20}$). The monoclinic phase can disappear with increasing the calcination temperature higher than 800 °C. The calcination of nano-oval composites at 600 °C exhibited a well crystalline degree, with sharp and high intensity peaks. Additionally, the average crystallite size (ca. 21–23 nm) of the $BaTi_{0.7}Fe_{0.3}O_3$ shielded $NiFe_2O_4$ nanocomposites, which was calculated from the Scherrer formula[20,21,42]. It is declared that the BTF is well shielded with the $NiFe_2O_4$ and has adequate stabilization.

The Rietveld analysis and the lattice parameters of the phases were given in Table 1. The XRD results indicated the good shielding of BTF nanoparticles in NFO NPs matrix, produced from the modification of BTF nanoparticles using NFO and calcination at 600 °C.

The X-ray density can be obtained from applying the following equation.[43–45]:

$$\rho_x = \frac{8M}{N_A V}$$

M is the molecular mass, V is the volume, and NA is the Avogadro number.

Morphological analysis using TEM. The particle nature of nano-oval $BaTi_{0.7}Fe_{0.3}O_3$ shielded with $NiFe_2O_4$ nanocomposites was investigated using transmission electron microscopy (TEM). Figures 4 showed the TEM images of the nano-oval $BaTi_{0.7}Fe_{0.3}O_3$ shielded with 5 $NiFe_2O_4$ nanocomposites. The results confirmed that the samples have nano-spherical and nano-ovals morphology (with the average size of 12 – 25 nm in diameter).The microstructures of the shielded ovals nanocomposite indicated that the BTFO phase is obviously described by regular grains, which are homogeneously distributed and connected with the NFO matrix. The samples showed a significant clustering to affect the XRD intensity. The occurrence of certain accumulated dark spots in the TEM images is due to the shielding of BTF with NFO and the interaction among magnetic NFO nanoparticles with the higher surface energies of the BTF. The crystal lattice displayed no clearly lattice deficiencies with clear boundaries. The internal distance between the two neighboring lattice planes is evaluated to be 0.292 nm associated with the main XRD peak of BTF and 0.235 nm associated with the main XRD peak of BTF@ NFO, which confirmed the successful shielding with the NFO nanoparticles. The TEM results indicated that the $NiFe_2O_4$ is highly shielded and well adhesion with the BTF nanoparticles. Moreover, the TEM data is supporting the XRD results. TEM images are evidence that the magnetic particle aggregation lies in the nanometric region.

Thermal study. The thermogravimetric test TGA is a technique that records the weight variations when a solid is warmed up at a uniform speed to evaluate its thermostability and volatile ingredient fraction. Since the object is processed under different conditions, the TGA technique falls under the category of thermal analysis[40]. The approach allows simultaneous measurement of the temperature, time, and mass of a sample in a managed flexible setting. These assessments are based on the fluctuation in weight of the material as a response to warm-

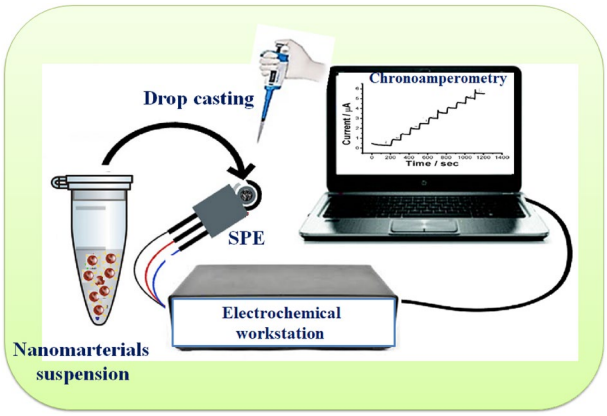

Figure 2. Steps of SPEs modification with 0B, 1B, 2B and 3B nanostructures before testing their electrochemical performance.

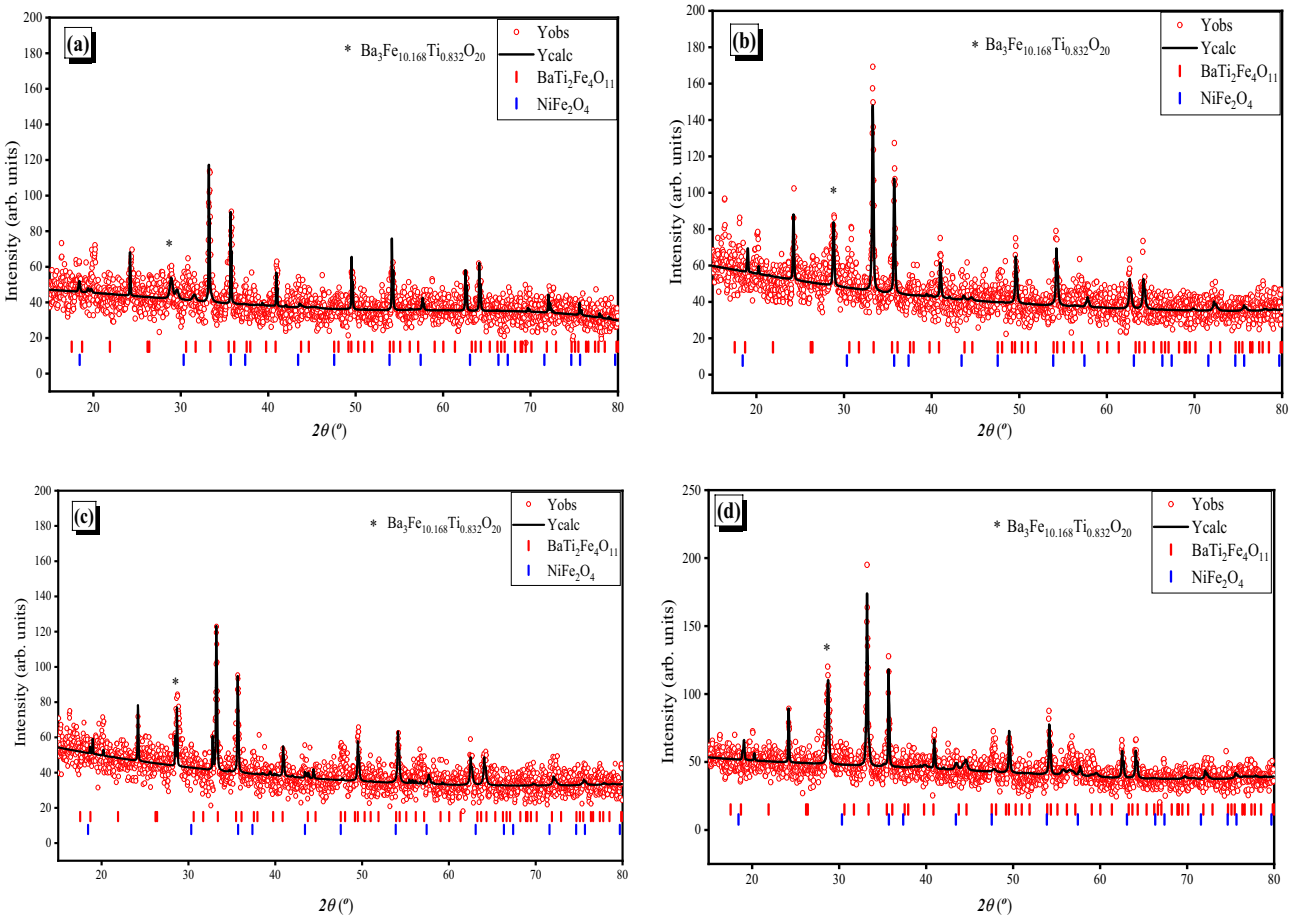

Figure 3. XRD patterns of (**a**) $BaTi_{0.7}Fe_{0.3}O_3$ shielded by $NiFe_2O_4$ NPs with concentrations (**b**) 1, (**c**) 3, and (**d**) 5 mol., calcined at 600 °C.

	$BaTi_2Fe_4O_{11}$ (hexagonal)					$NiFe_2O_4$ (cubic)			
Sample	a = b	c	Vol	α = β	γ	a = b = c	Vol	α, β, γ	ρ_x
0B	5.8432	13.604	402.253	90	120	8.3370	579.468	90	5.373
1B	5.8474	13.602	402.77	90	120	8.3408	580.261	90	5.366
2B	5.8462	13.612	402.938	90	120	8.3382	579.676	90	5.371
3B	5.8472	13.609	402.951	90	120	8.3406	580.219	90	5.366

Table 1. the lattice parameters for the formed phases.

ing a condition[46,47]. Therefore, a certain weight amount will be destroyed and evaluated as volatiles or decomposed, and this loss is detected with precision balance. The material is loaded in a cylinder pan built specifically for this testing. Temperature variations are determined by a tailored temperature program, which may include isothermal and ramp stages with varying warming levels[39]. The temperature of the cuvette is monitored using thermocouples in connection with it. For weight monitoring, the cuvette is normally put on a test stand which is attached to a mass-sensitive instrument. The sample holding cuvettes of a TGA device can be of various forms and compositions. They must be able to properly keep the sample, inert to it, and the heating conditions. Alumina, platinum, and aluminum are the most common materials used to make testing cuvettes[40]. An exhaust gas flowing into the oven creates an atmosphere that can be neutral, such as nitrogen or argon, oxidative, such as air or oxygen, or reductive, such as a mixture of hydrogen and nitrogen. The amount of moisture inside the oven could range from dry to saturated[40].

In this work, thermogravimetric analysis was carried out by TA instruments Lab Q5 in a nitrogen gas environment at temperatures ranging from 25 to 900 °C at a 10 °C/min heating rate. The TA Instruments Q50 TGA monitors the change in sample weight as a function of temperature. It employs delicate microbalance as well as precise heating management. The specimen mass limit is 1 g with an accuracy of 0.1 g.

The TGA curves of nanocomposites in the N_2 climate with a heating rate of 10 °C/min are shown in Fig. 5. The behavior shows two main decomposition reactions; the first one is mostly due to the dehydration and

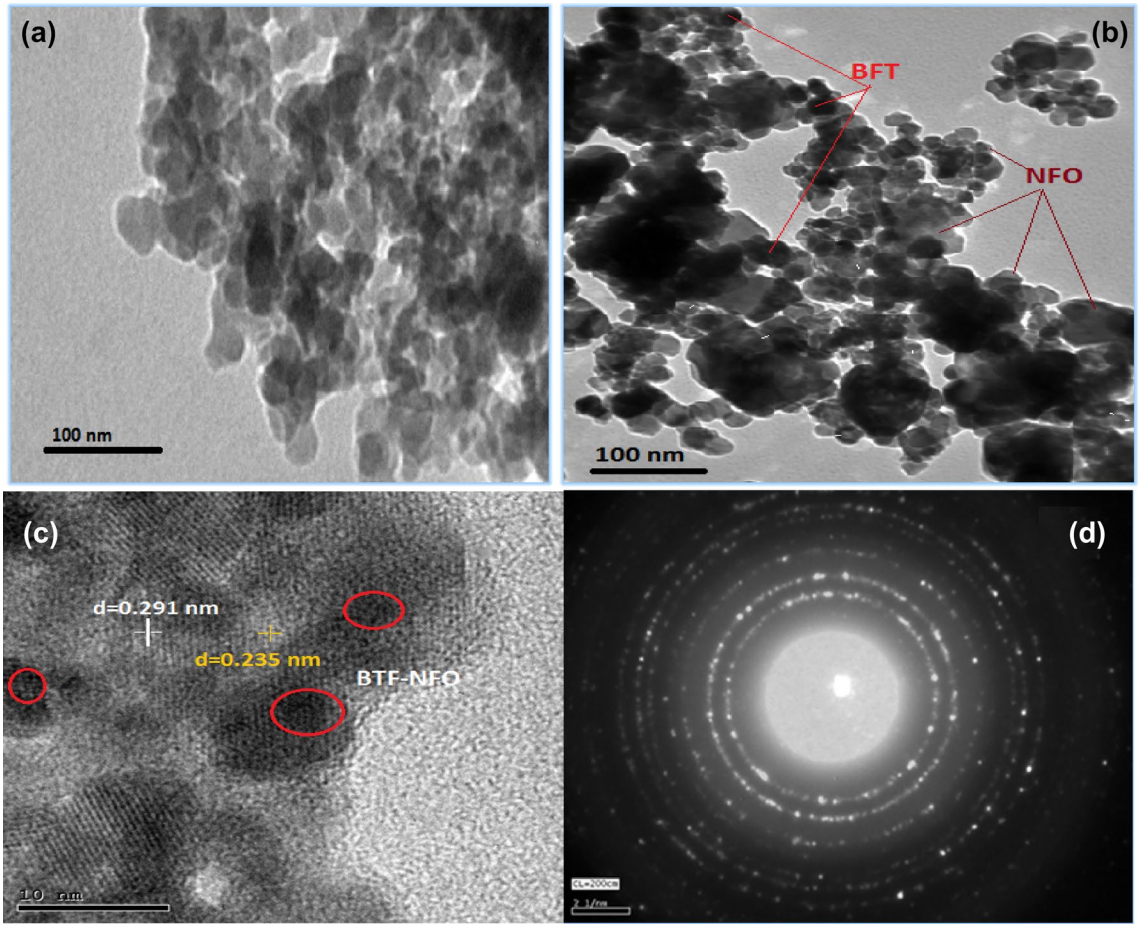

Figure 4. TEM images of nano-oval $BaTi_{0.7}Fe_{0.3}O_3$ and shielded with 5 $NiFe_2O_4$ nanocomposites, calcined at 600 °C.

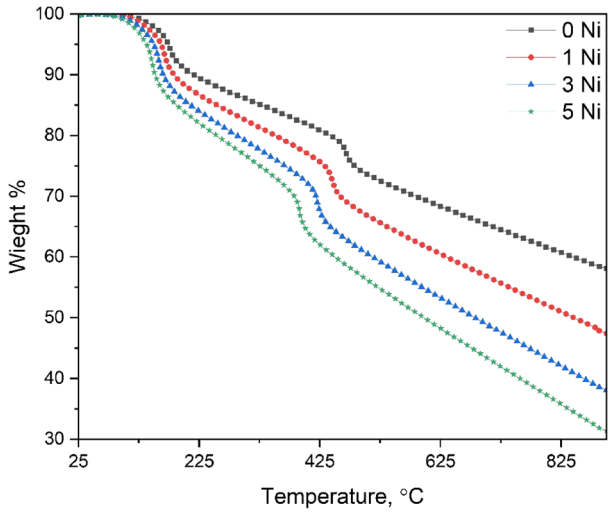

Figure 5. TGA curves of the prepared nanocomposites in the range of ambient to 900° C in an N_2 atmosphere with a heating rate of 10 °C/min.

evaporation of organic components[44,45]between (125–205 °C), (117–189 °C), (110–177 °C) and (97–167 °C) for the samples, respectively. The mass loss of 0, 0.1, 0.3, and 0.5 $NiFe_2O_4$ is approximately 9, 11, 13, and 14% of the initial weight, respectively. Because the range of events that occur in the first reaction decreases, the $NiFe_2O_4$ nanoparticle shells are not favorable to the thermal stability of the nanocomposites[45,48].

The second stage situated in the range of (457–481 °C), (434–460 °C), (412–434 °C), and (282–401 °C) for, 0.1, 0.3, and 0.5 $NiFe_2O_4$, respectively. This stage reflects the decomposition of the nanomaterial[43,48]. The samples (0.1, 0.3, and 0.5 $NiFe_2O_4$) loss was about 25, 30, 34, and 36% of their initial weight, respectively. The addition of $NiFe_2O_4$ nanoparticle shells led to a decrease in the range of occurrence of the process.

Diffuse reflectance. Diffused reflectance is the phenomenon resulting from reflection, refraction, diffraction, and absorption orientated in all directions. The discrete light absorption as well as the size-dependent are developed due to the confinement of quantum size[19]. In the case of nanocrystalline semiconductors, linear (one exciton per particle) and nonlinear (multiple excitons per particle) properties arise as a result of the transition from an electron and an electron hole to discrete (quantized) electronic shells. Optical absorption of the nano-sized oxides is influenced by nonstoichiometric defects which are size-dependent. In nanostructured oxides, the point defects concern the presence of dopant and/or the vacancies of cation or oxygen. In proportion to the number of defects, gap states are introduced by vacancy defects.

Diffuse reflectance was used to study the optical properties of the prepared $BaTi_{0.7}Fe_{0.3}O_3$/(0, 1, 3, 5) $NiFe_2O_4$ (BTFO/NFO) nanocomposites in the wavelength range of 200 to 2500 nm, as shown in Fig. 6. The diffuse reflectance of all samples increases with wavelength increase until about 1870 nm, where the interference takes place.

Furthermore, in Fig. 6a, the increase in $NiFe_2O_4$ leads to a decrease in diffuse reflectance values. Previously[49], it was observed that the absorption spectrum of the BTO exhibits a sharp absorption edge above 3 eV and peaks at 3.51 eV roughly taken as the value of the band gap, that is, 3.51 eV. This edge corresponds to the band-to-band absorption scenario in the 'extrinsic band insulator of the tetragonal $BaTiO_{3-\delta}$[49]. In that case, the oxygen deficiency content δ, which is quite small, can be qualitatively reflected from a long tail below the rising edge in the range of photon energies between 2 and 3 eV[49]. In the current work, the absorption spectrum of the BTFO becomes broadening (Fig. 6b), which spans a wide range of photon energies from the ultraviolet region to the near-infrared one. This spectrum can be spectroscopically de-convoluted into two Lorentzian components as shown in Fig. 6b, whose peaks are at about 340 nm and 520 nm, respectively. The first component may be attributed to a combination of multiple absorption processes to donor levels in the forbidden band[49].

However, the second component is due to band-to-band absorption for hexagonal BTFO, i.e., Fe-doped hexagonal BTO, with a band gap Eg 2.7 eV smaller than that of the undoped tetragonal BTO (Eg ≈ 3.51 eV)[49]. In addition, the red shift observed for UV–VIS absorption spectra is a direct consequence of the change of the band structure from the tetragonal BTO crystal to the hexagonal BTFO one, which is caused by substituting the Fe ion for Ti^{4+} to create Fe ions with an oxidation state of about 3.92 and positively charged oxygen vacancies as the electron trapping centers.

The method of Kubelka and Munk (K–M) was employed to determine the optical band gap (Eg) of the BTF/NiFO materials, which is based on the conversion of the diffused reflectance measurements. The Kubelka–Munk equation is given below for a specific wavelength:

$$F(R_d) = \left(\frac{k}{s}\right)(1 - R_d)^2/2R_d \tag{1}$$

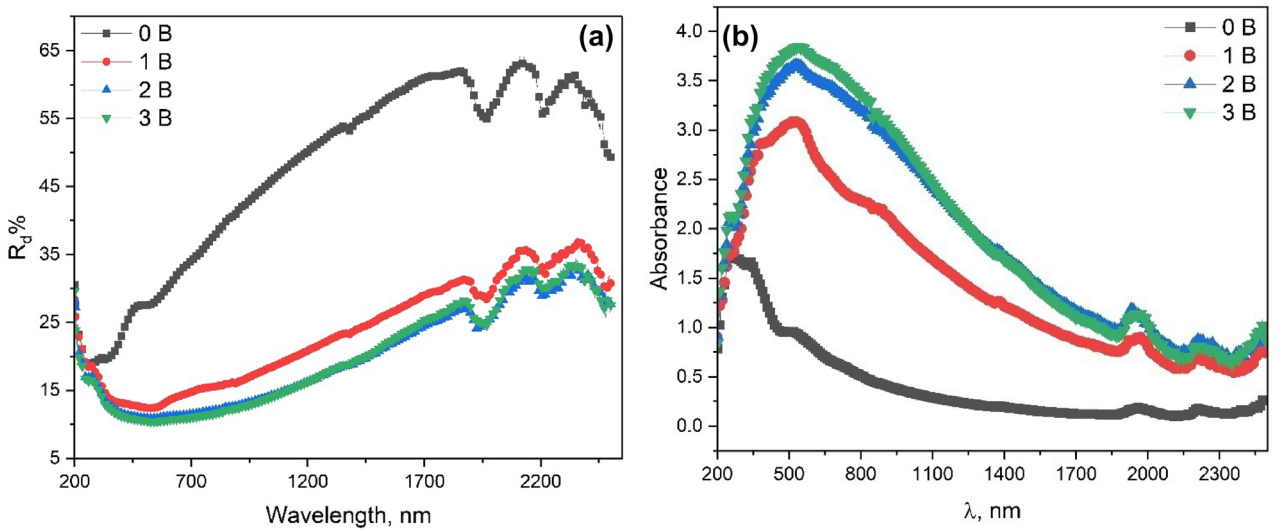

Figure 6. (**a**) Diffuse reflectance and (**b**) absorptance spectra of $BaTi_{0.7}Fe_{0.3}O_3$/(0, 0.1, 0.3, 0.5) NiFe2O4 nanocomposites in the wavelength range of 200 to 2500 nm.

where $F(R_d)$ is the K–M function or the absolute reflectance of the material. In reflectance measurements, barium sulphate ($BaSO_4$) is used as a standard sample. 'k' is the coefficient of molar absorption and 's' is the scattering coefficient. The relation between the optical band gap and the absorption coefficient of semiconductor oxide materials was determined by Wood and Tauc in the case of a parabolic band structure. According to them, the following equation is based on the optical band gap in absorption and photon energy[50]:

$$F(R_d)h\nu = C\left(h\nu - E_g\right)^n \tag{2}$$

where 'α' is the absorption coefficient of the samples and 'hυ' is the photon energy. C is the constant factor, E_g is the optical band gap, and 'n' is a constant correlated with various types of electronic transition (n = 1/2 for a direct allowed transition, n = 2 for an indirect allowed, n = 3/2 for a direct forbidden, and n = 3 for an indirect forbidden transition) as previously reported in the literature[19,51].

The BTFO/NiFO nanocomposites show an optical absorption spectrum caused by the direct and indirect electronic transition with a higher probability of the direct one. In the direct mechanism, electrons in the higher energy state in a VB move to the lowest energy states in the CB under the same point in the Brillouin zone after the electronic absorption process[52,53]. Therefore, by plotting and extrapolating a graph between $[F(R)\ h\upsilon]^n$ and hυ for n = 2 and 1/2, E_g values corresponding to the different concentrations of Ni-ion in BTFO samples are calculated by the linear portion of the curve (Fig. 7a and b). Figure 7c, the Eg values measured to be 1.021, 0.289, 0.289, and 0.289 eV for BTFO/xNiFO (x = 0.0 to 0.5) nanocomposites in the direct case, and 2.674, 1.482, 1.482, and 1.482 eV in the indirect case. This gap is due to the presence of intermediate energy levels for both the valence band (VB) and conduction band (CB). In the case of Ni-doped BTFO materials, the Eg values decrease with doping. The incorporation of Ni ion BTFO introduces 'B-site' vacancies, which contribute to structural deformation and distortion[49,53]. These vacancies of the 'B site' introduce shallow defects in the optical band gap

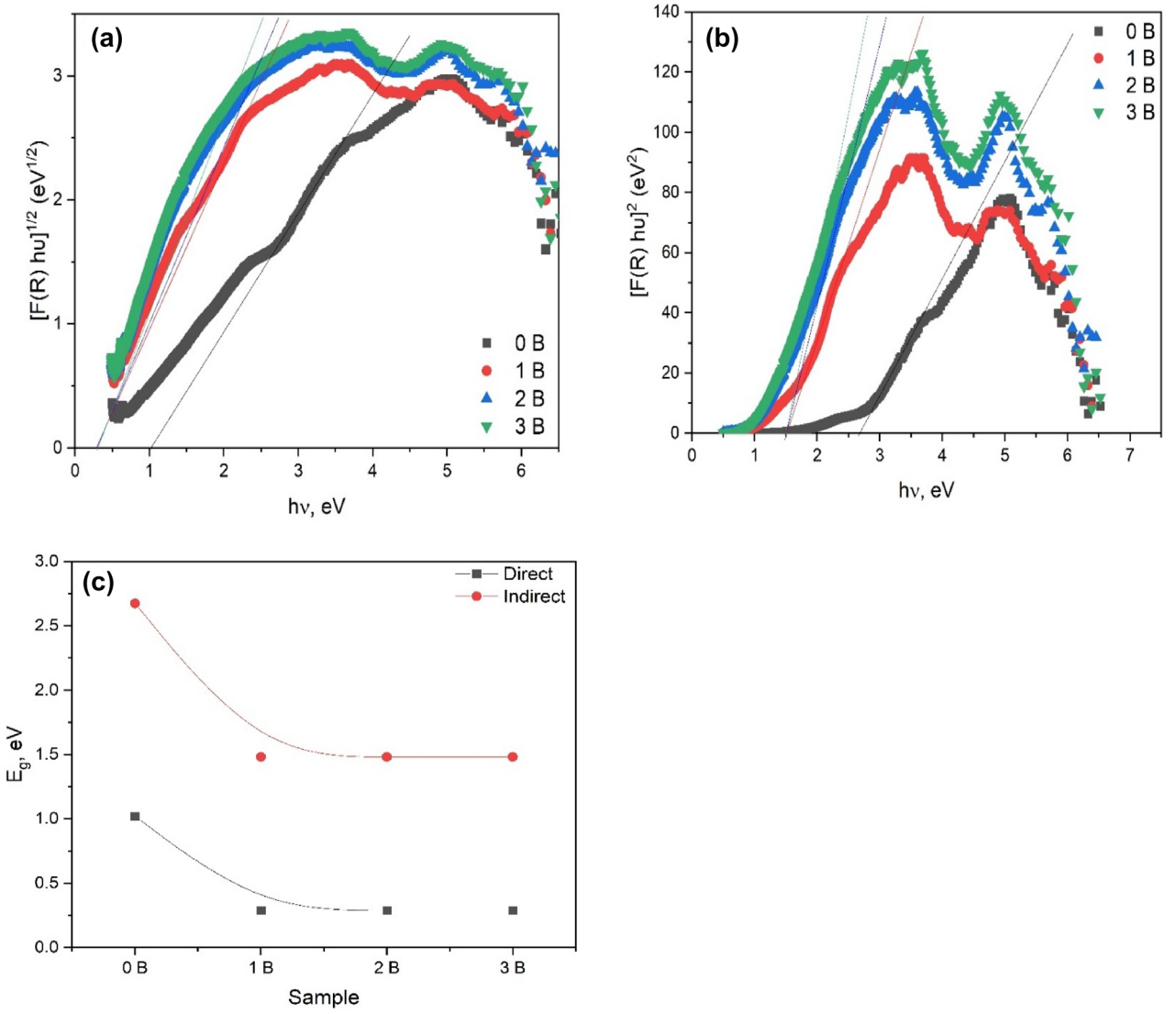

Figure 7. Plot of $[F(R)\ h\upsilon]^n$ and hυ for (**a**) n = 2 and (**b**) n = 1/2, and (**c**) the behavior of energy band gap with the Ni content in both direct and indirect cases.

and therefore the Eg value decreases. The B-site vacancies increase with the doping and resulting in the creation of the free carriers that have a many-body effect, which reduces electron energy as compared to a noninteracting carrier network. Such interaction can take the form of interaction between electron–electron, electron-donor, electron–hole, hole-hole, and hole-acceptor[49,53].

The material refractive index is known to minimize with energy gap. Consequently, both these common quantities are thought to have a particular relationship. There were different efforts to locate an acceptable correlation (empirical and semiempirical) between the refractive index and the energy gap of semiconductors. Some of these attempts are the Moss relation and Vandamme relation[54,55]. The claimed relationships have already been presented with justifications for obtaining a satisfactory agreement to experimental results[54,55] and so it will be used here to calculate the refractive index of the prepared samples from the obtained energy gaps.

Figure 8a shows the change of the refractive index with Ni content calculated by different attempts described before for direct and indirect transition cases. It is obvious that there are small differences between the n values calculated by different methods and this may be due to the difference in the mathematical approximation methods used in every attempt. Also, the refractive index increases by NFO addition, and then the behavior is kept constant with NFO content increasing. This means that the prepared nanocomposites are desirable in applications that need a constant refractive index such as military applications, space, and optical devices.

The material dielectric constant is linked to the refractive index[54] by ($\varepsilon_\infty = n^2$). The dielectric constants of the prepared samples are given in Fig. 8b for direct and indirect gap cases respectively. It was noted that the dielectric constant change behavior with Ni change is similar to the behavior of the refractive index.

Duffy[56] has demonstrated the earlier view and presented it as optical electronegativity ($\Delta\chi^*$) and get the formula that links it by energy gap ($\Delta\chi^* = 0.2688E_g$). The Duffy relation is used in calculating the optical electronegativity of the prepared samples for the direct and indirect transition gaps, and the resulting values

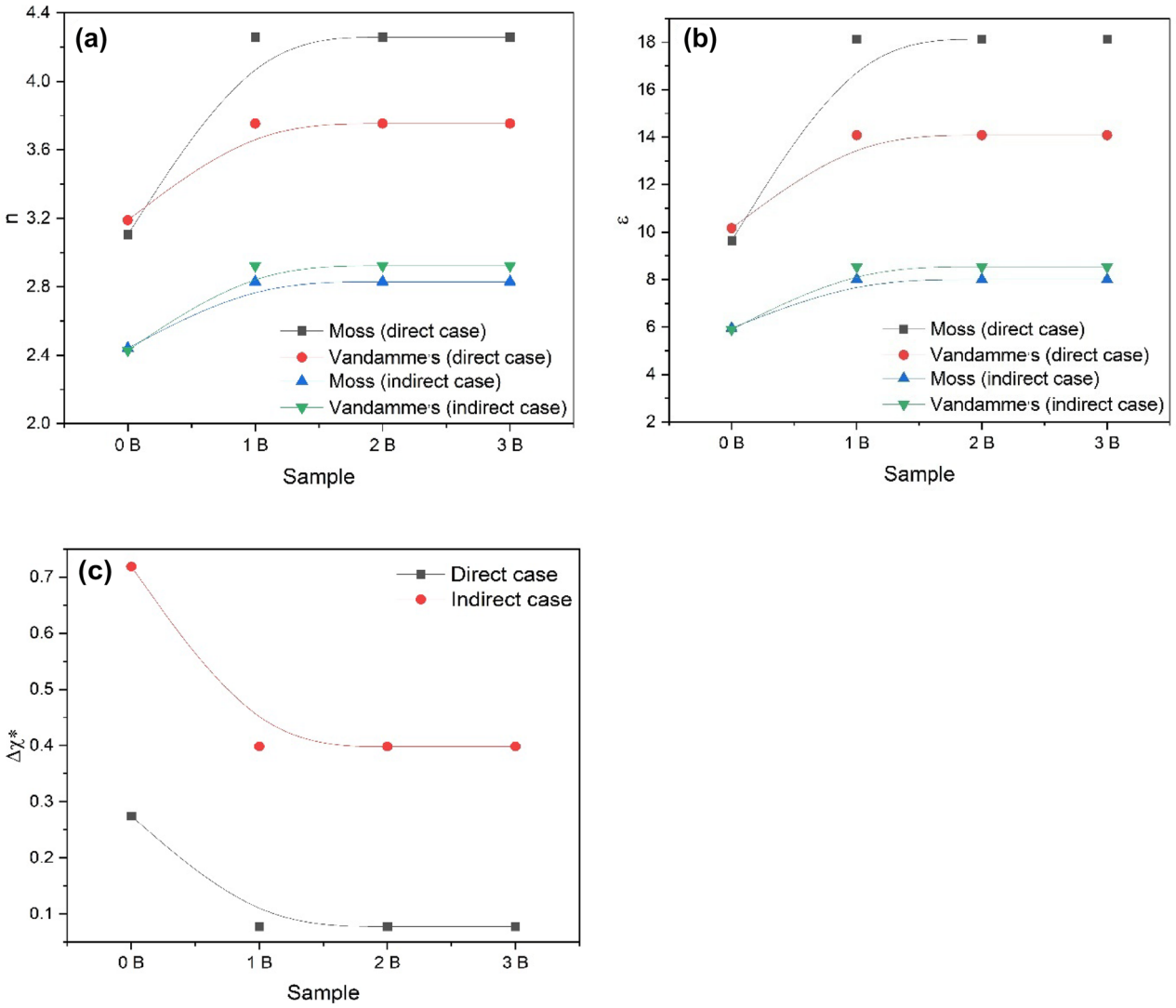

Figure 8. (**a**) Refractive index, (**b**) Optical dielectric constant, and (**c**) Electronegativity of $BaTi_{0.7}Fe_{0.3}O_3$/(0, 1, 3, 5) $NiFe_2O_4$ nanocomposites in the wavelength range 200–2500 nm.

were presented in Fig. 8c. The presented data shows that the BTFO/NiFO optical electronegativity lies between (0.7–0.07) for both direct and indirect cases, respectively. Following Pauling's[57] indication, the current samples are covalent as predicted by XRD.

Magnetic properties. Figure 9 shows the magnetic hysteresis loop of iron barium titanate shielded with nickel ferrite (nano-oval $BaTi_{0.7}Fe_{0.3}O_3$ shielded (0.1, 0.2, 0.5) $NiFe_2O_4$) nanocomposites. The M–H curve of the composites exhibits a saturated magnetic hysteresis loop that the composites samples have a ferromagnetic nature. This hysteresis loop for all samples is small, which is a specific feature for a soft ferrite $NiFe_2O_4$.The composites gained their magnetic property from the presence of the ferromagnetic phase ($NiFe_2O_4$). The magnetic nature of $NiFe_2O_4$ nanopowder results from the antiparallel distribution of the magnetic centers (Ni^{2+} and Fe^{3+}) between the octahedron and the tetrahedron sites. Therefore, increasing the concentration of the ferromagnetic phase (NF) in the composite increases the magnetic centers in the composite samples, and hence the total magnetic moment of the samples increases too. Therefore the saturation magnetization of the composites increases with increasing the NF concentration. The diamagnetic phase BTF decreases the interaction between the magnetic centers NF and hinders the rotation of the magnetic centers with the applied magnetic field, therefore the saturation magnetization decreases with increasing the diamagnetic phase concentration[58,59]. The magnetic parameters (saturation magnetization Ms, Remanent magnetization Mr, and coercive field Hc) of the composites are listed in the inset of Fig. 9 to highlight that increasing the ferrite content in the composite improves the magnetic properties of the composites. This can be explained on the basis of the presence of Ni^{2+} and Fe^{3+} ions present in the $NiFe_2O_4$ system as a coated layer. Since the increase of their contents may be causing the increase of their unit cell, thereby increasing the lattice parameter and exchange interactions within A and B sites. Also, the presence of Fe3 + in the based BaTi0.7Fe0.3O3 and in the NFO layer enhances the magnetization of the B-site.

Dielectric (relative dielectric permittivity). The relative dielectric permittivity (ε'(ν)) of the composite samples (BTF/xNFO) against temperature at different frequencies is shown in Fig. 10. As a result, an increasing behavior in the dielectric permittivity with increasing temperature was obtained until a critical temperature. Then, a decrease in the dielectric permittivity was observed with higher temperatures. This critical temperature is the Curie temperature and represents the transition from the ferroelectric to the para-electric state. According to Fig. 10, the BTF sample has two transition temperatures; the first transition is assigned to the presence of an unstable monoclinic phase, while the second one represents the ferroelectric transition temperature.

Electrochemical properties. Electrochemical behaviors of the prepared nanocomposite are identified, in a stranded redox mediator of ferro/ferricyanide, by cyclic voltammetry (CV) and electrochemical impedance spectroscopy (EIS). As a result, a fast oxidation–reduction and highest faradic current of the standard redox probe were obtained for all nanocomposite-based electrodes (0, 1, 2 and 3B), as presented in Fig. 11a and b. The ascending order in the voltammetric signals is as follows: 3B > 2B > 1B > 0B, as depicted in Fig. 11a and Table 2. Therefore, the highest conductivity alongside electrochemical activity is dedicated to the modification of electrode surface with the nanocomposite (3B).

In parallel to the voltammetric studies, EIS analysis was conducted for all modified electrodes, as displayed in Fig. 11b, and Table 2. Nyquist plots, at high frequency, showed a semicircle portion reflecting the changes in the electron transfer resistances, whereas the charge transfer resistance (R_{ct}) at the electrode interface was presented by the diameter of the semicircle. Matching with the voltammetric results, the lowest resistances were obtained from 3B-based electrode (Rct = 88.4Ω) followed by 2B (R_{ct} = 148.7Ω), 1B (Rct = 231.2 Ω), and 0B (Rct = 407.8Ω). Worth mentioning here that the all composite-based electrodes provided lower charge transfer resistances than that obtained by the unmodified electrodes (Rct = 1400.8 Ω). The inset in Fig. 11b represents the equivalent circuit used for fitting the impedance Nyquist plots. From the CV and EIS results, we could conclude that the 3B composite has a promising property and can be exploited in electrochemical applications.

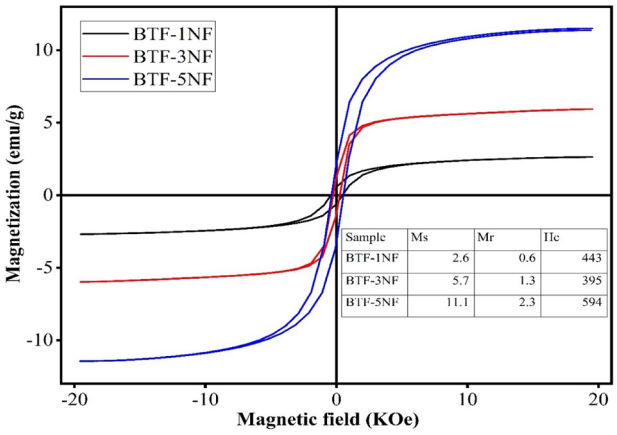

Figure 9. Magnetic hysteresis loops of iron barium titanate (BTF) shielded with nickel ferrite (BTF/xNFO).

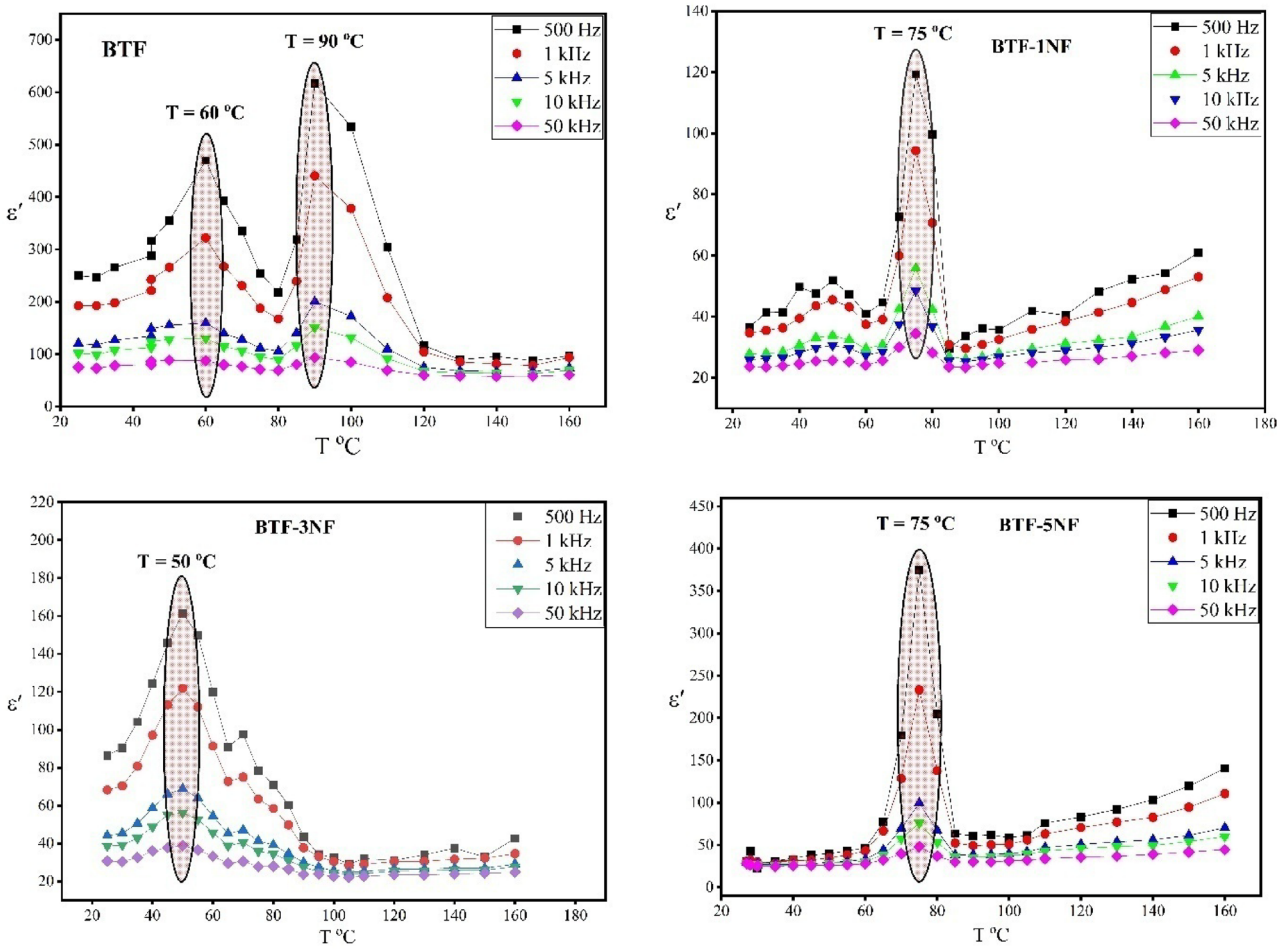

Figure 10. Relative dielectric permittivity (ε'(ν)) versus temperature at different frequency of iron barium titanate (BTF) and iron barium titanate shielded with nickel ferrite (BTF/xNFO).

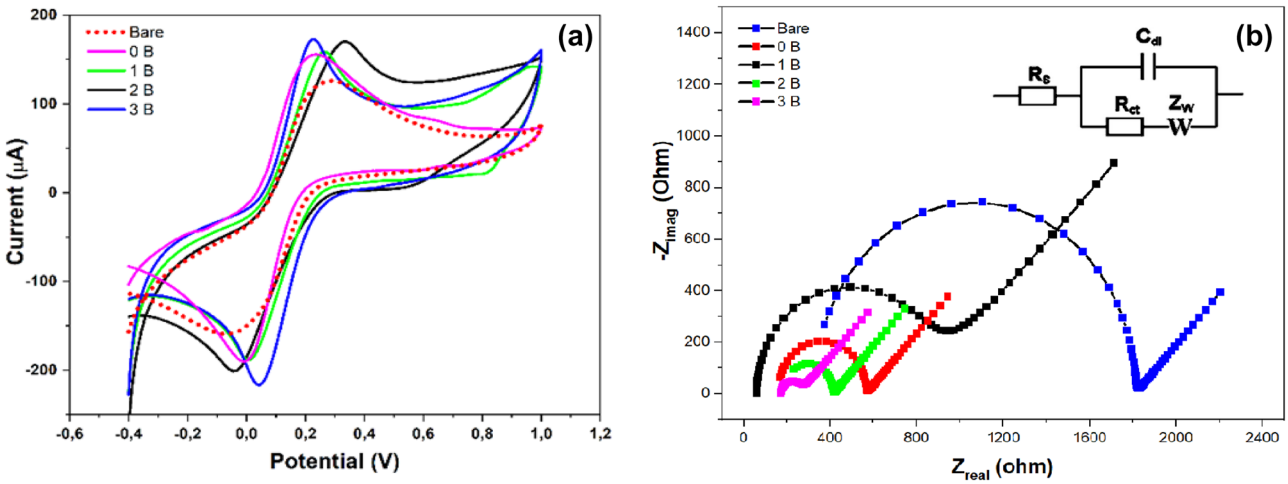

Figure 11. (**a**) CV measurements of (Bar, 0, 1,2 and 3 B) were conducted in a solution of standard redox probe of ferricyanide with the 5 mM in KCl as the supporting electrolyte. Scan rate of 50 mV s^{-1} was applied for all experiments. (**b**) Show EIS Nyquist spectra characterization of modified electrodes with the nanomaterials. The inset represent the modeled Circuit thatis used for curve fitting.

Electrode type	I_a (µA)	I_c (µA)	$E_{oxd.}$ (V)	$E_{red.}$ (V)	$E_{1/2}$ (V)	R_s (Ω)	$R_{ct\ (1)}$ (Ω)	C µF	W (Ω)
Bare	124	−158	0.274	−0.06	0.107	324	1400	0.136	0.0028
0 B	153	−188	0.233	−0.05	0.09	159	407	0.243	0.0023
1 B	159	−189	0.268	0.01	0.139	184	231	0.432	0.02216
2 B	169	−202	0.334	−0.03	0.152	126	148	0.573	0.00227
3 B	171	−216	0.227	0.045	0.136	173	88	1.231	0.0020

Table 2. The electrochemical parameters (CV & EIS) obtained for the modified electrodes with the prepared nanomaterials. Those values are extracted from the above discussed voltammetric as well as the impedimetric experiments (Fig. 11).

The redox peaks which appeared in the CV curves for prepared nanocomposites showed a pseudocapacitive electrode material significant feature. In the charge/discharge process, very fast reversible faradaic redox occurred along with the faradaic charge transfer and intercalation of protons at the surface of the electrodes. The effect of scan rate on the electrochemical behavior of each prepared nanomaterial (0, 1, 2, and 3B) was studied by the cyclic voltammetry method (Fig. 12A, B, C and D). In the scan rate range from 0.01 to 1.0 V/s, the redox peak currents (i_{pa} and i_{pc}) increased as the scan rate increased for 0, 1, 2, or 3B modified electrodes. In Fig. 13, the lower electrical conductivity of 0B is due to lower peak current values. On the other hand, the values of peak current increased in 1B and 2B.The highest peak current values were observed in 3B, which refers to its capacitive properties. However, the cyclic voltammogram exhibited a well-known hysteresis-type loop, which is significant for a supercapacitor. Furthermore, all prepared nanomaterials were stable electrochemically over various applied scan rates, and no damage was produced in the electrode-modified composition.

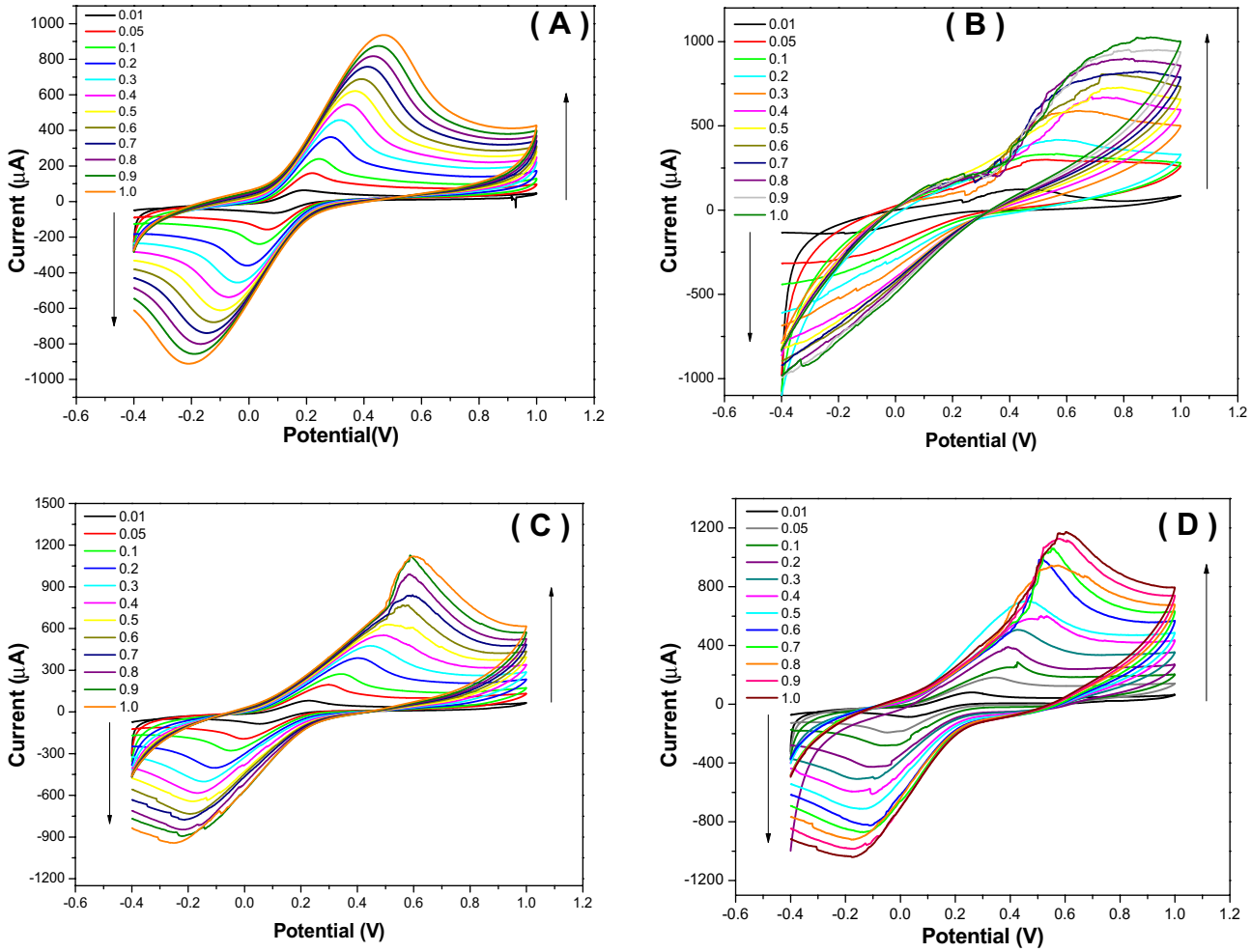

Figure 12. CV of prepared nanocomposites (**A**) 0B, (**B**)1B, (**C**)2B, and (**D**) 3B at different scan rates. Screen printed electrodes were modified with a thin film of the nanomaterials and voltammetric experiments were performed in the ferricyanide (5 mM).

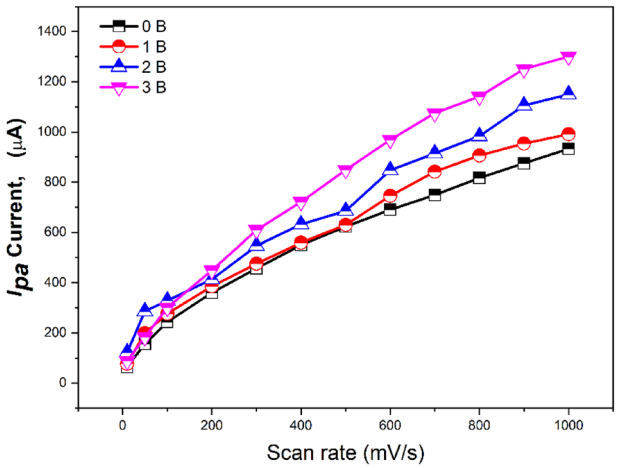

Figure 13. Influence of scan rate changes on the oxidation currents of the 0B, 1B, 2B and 3B nanostructure-based electrodes at different scan rate.

The use of 0B, 1B, 2B and 3B nanostructures for H_2O_2 detection. The electrochemical properties of nanocomposite materials modified electrode is one of the key benefits to supply high electrocatalytic activity which produces fast electron transfer and direct oxidation in the field of non-enzymatic biosensors. Therefore, the study of direct electron transfer produced from the oxidation of hydrogen peroxide evaluated overall prepared nanomaterials. The direct oxidation was measured by CV and chronoamperometric methods by adding different peroxides concentrations into the electrochemical cell. The cyclic voltammetry graph and a calibration curve are represented in Fig. 14a and chronoamperometric calibration curves of bare, 0B, 1B, 2B, and 3B modified electrodes are shown in Fig. 14b. The highest signals were obtained by the 3B modified electrode. Therefore, the high electrocatalytic activity of 3B allowed the direct electrochemical oxidation of peroxide. In addition, as the concentration of H_2O_2 increased, an increase in oxidation peak currents were produced which revealed the high sensitivity and reliability of the 3B modified SPE.

Consequently, the amperometric signal of peroxide oxidation at different pHs was studied. As represented in Fig. 14c), the amperometric response of the 3B-based electrodes towards the peroxide's oxidation was measured at different pHs, and the electrochemical signal increased as the pH increased from 4 up to 7 then decreased above pH = 7.0. So that, PBS buffer with pH 7.0 was selected for all subsequent experiments.

Amperometric detection of peroxide. From cyclic voltammetry (CV) detection, the peroxide oxidation peak was produced at 0.7 V. Therefore, the amperometric study was evaluated at 0.7 V by adding a standard concentration of H_2O_2 at a fixed time (100 s). Figure15 showed the relation between the different concentrations of peroxides and current response with a fast and high response, which approved the fast electron transfer due to the electro-catalytic behavior of the 3B-based electrodes. The calibration curve (as it is clear in Fig. 15) showed a linear range from 0.1 up to 650 μM with a detection limit of 0.01 μM, which approved the high sensitivity of the proposed electrode to be effectively applied in the non-enzymatic-based biosensors field. Additionally, a comparison of electrochemical response between electrochemical performance of the newly developed electrode for peroxide determination and the other reported materials is tabulated in Table 3.

Conclusion

From this work, activated $NiFe_2O_4$ nano-oval was successfully shielded with $BaTi_{0.7}Fe_{0.3}O_3$ nanoperovskite synthesized via the sol–gel chemical manner and calcined at 600 °C. The XRD powder asserted the formation of biphases for pero-$NiFe_2O_4$ nanocomposites. The measured band gap energy was 1.021, 0.289, 0.289, and 0.289 eV in the direct case, and 2.674, 1.482, 1.482, and 1.482 eV in the indirect case, respectively for BTFO/xNiFO (x = 0 to 5) nanocomposites. The incorporation of Ni ion into BTFO introduces 'B-site' vacancies, which contribute to structural deformation and distortion. . With the addition of Ni ion, the electronegativity exhibits a behavior similar to that of the band gap, but the refractive index and optical dielectric constant exhibit opposite behavior. The addition of $NiFe_2O_4$ plays an appreciable role in enhancing temperature stability and increasing the permittivity of the pero-magnetic $BaTi_{0.7}Fe_{0.3}O_3$@ $NiFe_2O_4$ nanocomposites. The pero-magnetic $BaTi_{0.7}Fe_{0.3}O_3$@ $NiFe_2O_4$ nanocomposite electrode has been used as a sensing material for H_2O_2 detection. The results of electrochemical data approved that the new $BaTi_{0.7}Fe_{0.3}O_3$@$NiFe_2O_4$ nanocomposites can be used effectively to direct H_2O_2-detection in biological analysis such as enzymatic-based sensors. Eventually, the obtained results are of excessive value to progress the structural, morphological, thermal, electrical, and electrochemical properties of pero-nanomagnetic composites at different calcination and ferrites contents, which enable be projected to apply in various applications as catalytic, biosensors, electromagnetic interference shielding systems, …. etc.

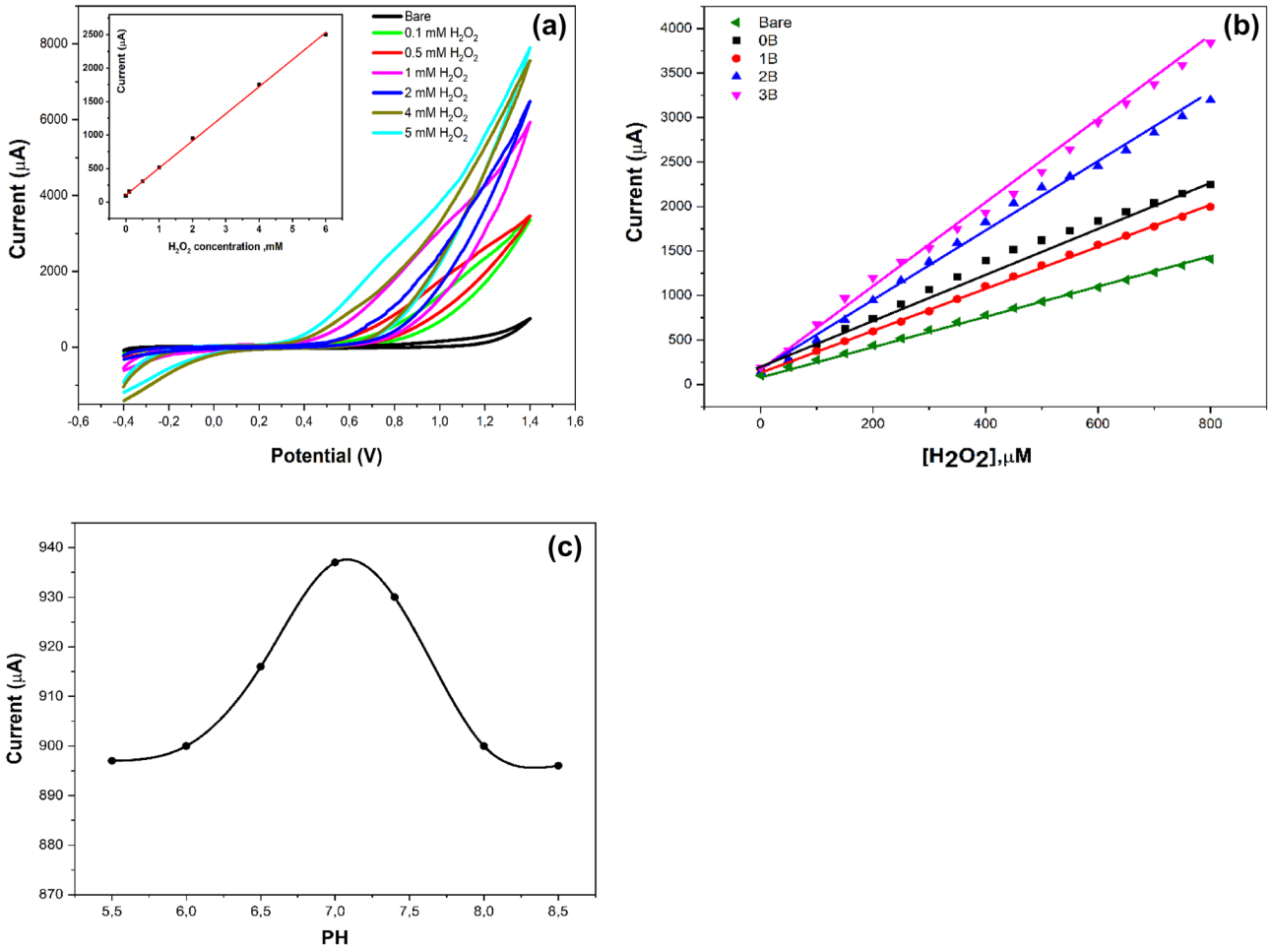

Figure 14. (**a**) Cyclic voltammety of 3B-based electrodes towards the direct voltammetric oxidations of different concentrations of H_2O_2 in (PBS pH = 7.0). The calibration curve is presented in the inset figure. (**b**) Chronoamperometric calibration curves of bare, 0B, 1B, 2B, and 3B toward different concentrations of H_2O_2 in (PBS pH = 7.0). (**c**) pH effect on the sensor performance towards the sensitivity of direct peroxides detection.

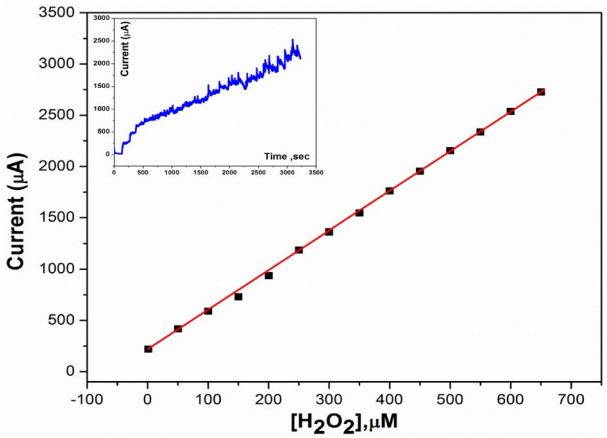

Figure 15. The corresponding calibration curve toward H_2O_2 response.

Electrode	Linear range (μM)	Detection limit (μM)	Applied potential (V)	Ref
Poly(azureA)PtNPs/SPCE	0–300	0.052	0.1	[60]
Co_3O_4-rGO	15–675	2.4	− 0.19	[61]
rGO-Pt	0.5–3475	0.2	− 0.08	[62]
Pt/rGO-CNT paper electrode	0.1–25	0.01	− 0.25	[63]
Co_3O_4/SPCE	0.1–50	0.145	1.0	[64]
$MnCo_2O_3$/CNTs/SPE	0.1–180	0.1	0.7	[24]
$BaTi_{0.7}Fe_{0.3}O_3$@$NiFe_2O_4$	0.1–650	0.01	0.70	This work

Table 3. Comparison of the analytical performance of various Hydrogen Peroxide Sensors (with various literatures). *Screen printed carbon electrode *SPCE*, Screen-printed electrode *SPE*, *NPs* Nano plates.

Data availability

Additional information Correspondence and material requests should be addressed to A.M. El Nahrawy (amany_physics_1980@yahoo.com. am.elnahrawy@nrc.sci.eg).

Received: 16 February 2023; Accepted: 29 May 2023
Published online: 03 June 2023

References

1. Rajan, S., Gazzali, P. M. M. & Chandrasekaran, G. Electrical and magnetic phase transition studies of Fe and Mn co-doped BaTiO3. *J. Alloys Compd.* **656**, 98–109 (2016).
2. Ren, X. *et al.* Room-temperature multiferroicity and magnetoelectric couplings in (Co0.75Al0.25)2(Fe0.75Mg0.25)O_4 spinel films. *J. Alloys Compd.* **920**, 165918 (2022).
3. Lone, I. H. *et al.* Multiferroic ABO_3 transition metal oxides: A rare interaction of ferroelectricity and magnetism. *Nanoscale Res. Lett.* **14**, 1–12 (2019).
4. Mangalam, R. V. K., Ray, N., Waghmare, U. V., Sundaresan, A. & Rao, C. N. R. Multiferroic properties of nanocrystalline $BaTiO_3$. *Solid State Commun.* **149**, 1–5 (2009).
5. Gajula, G. R., Buddiga, L. R. & Dasari, M. Influence of Gd/Nb on activation energy, relaxation response, impedance, Nyquist plots and dielectric studies at high frequency of $BaTiO_3$-Li0.5Fe2.5O_4 solid compounds. *Results Phys.* **18**, 103196 (2020).
6. Kundu, T. K., Jana, A. & Barik, P. Doped barium titanate nanoparticles. in *Bulletin of Materials Science* vol. 31 501–505 (Springer, 2008).
7. Chen, X. *et al.* Influence of transition metal doping (X = Mn, Fe Co, Ni) on the structure and bandgap of ferroelectric Bi 3.15Nd 0.85Ti_2 X_1O_{12}. *J. Phys. D. Appl. Phys.* **50**, 105104 (2017).
8. Atta, N. F., Galal, A. & El-Ads, E. H. Perovskite nanomaterials synthesis, characterization, and applications. *Perovskite Mater. Synth. Characterisation Prop. Appl.* https://doi.org/10.5772/61280 (2016).
9. Spasojevic, I., Sauthier, G., Caicedo, J. M., Verdaguer, A. & Domingo, N. Oxidation processes at the surface of $BaTiO_3$ thin films under environmental conditions. *Appl. Surf. Sci.* **565**, 150288 (2021).
10. Wegmann, M., Watson, L. & Hendry, A. XPS analysis of submicrometer barium titanate powder. *J. Am. Ceram. Soc.* **87**, 371–377 (2004).
11. Tuan Sulong, T. A., Maulat Osman, R. A., Idris, M. S. & Zahid Jamal, Z. A. Structural and electrical properties of barium titanate ($BaTiO_3$) and neodymium doped $BaTiO_3$ (Ba0.995Nd0.005TiO3). *EPJ Web Conf.* **162**, (2017).
12. Billah, M. *et al.* Microstructure evolution and electrical characterization of lanthanum doped barium titanate ($BaTiO_3$) ceramics. *AIP Conf. Proc.* **1754**, (2016).
13. Abdel Aal, A., Hammad, T. R., Zawrah, M., Battisha, I. K. & AbouHammad, A. B. FTIR study of nanostructure perovskite $BaTiO_3$ doped with both Fe_3+ and Ni_2+ ions prepared by sol-gel technique. *Acta Phys. Pol. A* **126**, 1318–1321 (2014).
14. Verma, K. C. & Kotnala, R. K. Multiferroic approach for Cr, Mn, Fe Co, Ni, Cu substituted $BaTiO_3$ nanoparticles. *Mater. Res. Express* **3**, 055006 (2016).
15. Maikhuri, N., Panwar, A. K. & Jha, A. K. Investigation of A- and B-site Fe substituted $BaTiO_3$ ceramics. *J. Appl. Phys.* **113**, 17D915 (2013).
16. Das, S. K., Rout, P. P., Pradhan, S. K. & Roul, B. K. Effect of equiproprotional substitution of Zn and Mn in BaTiO3 ceramic—An index to multiferroic applications. *J. Adv. Ceram.* **1**, 241–248 (2012).
17. Liu, G., Wang, K., Gao, X., He, D. & Li, J. Fabrication of mesoporous NiFe2O4 nanorods as efficient oxygen evolution catalyst for water splitting. *Electrochim. Acta* **211**, 871–878 (2016).
18. Amulya, M. A. S. *et al.* Sonochemical synthesis of NiFe2O4 nanoparticles: Characterization and their photocatalytic and electrochemical applications. *Appl. Surf. Sci. Adv.* **1**, 100023 (2020).
19. ElNahrawy, A. M. *et al.* Impact of Mn-substitution on structural, optical, and magnetic properties evolution of sodium–cobalt ferrite for opto-magnetic applications. *J. Mater. Sci. Mater. Electron.* **31**, 6224–6232 (2020).
20. El Nahrawy, A. M., Hemdan, B. A., AbouHammad, A. B., Abia, A. L. K. & Bakr, A. M. Microstructure and antimicrobial properties of bioactive cobalt co-doped copper aluminosilicate nanocrystallines. *SILICON* **12**, 2317–2327 (2020).
21. AbouHammad, A. B., Darwish, A. G. & El Nahrawy, A. M. Identification of dielectric and magnetic properties of core shell $ZnTiO_3$/$CoFe2O_4$ nanocomposites. *Appl. Phys. A* **126**, 504 (2020).
22. Haddad Irani-nezhad, M., Hassanzadeh, J., Khataee, A. & Orooji, Y. A chemiluminescent method for the detection of $H2O_2$ and glucose based on intrinsic peroxidase-like activity of WS_2 quantum dots. *Molecules* **24**, 689 (2019).
23. Tian, R. *et al.* Fluorometric enhancement of the detection of H_2O_2 using different organic substrates and a peroxidase-mimicking polyoxometalate. *RSC Adv.* **9**, 12209–12217 (2019).
24. Yousf, N. *et al.* Synthesis, characterization, and electrochemical sensing applications of bimetallic oxide/carbon nanomaterials hybrids. *J. Electrochem. Soc.* **169**, 047518 (2022).
25. Rhee, S. G., Chang, T.-S., Jeong, W. & Kang, D. Methods for detection and measurement of hydrogen peroxide inside and outside of cells. *Mol. Cells* **29**, 539–549 (2010).
26. Salih, E., Mekawy, M., Hassan, R. Y. A. & El-Sherbiny, I. M. Synthesis, characterization and electrochemical-sensor applications of zinc oxide/graphene oxide nanocomposite. *J. Nanostructure Chem.* **6**, 137–144 (2016).

27. Tohamy, H.-A.S. & Magar, H. S. A flexible, low-cost, disposable non-enzymatic electrochemical sensor based on MnO_2/Cellulose nanostructure. *ECS J. Solid State Sci. Technol.* https://doi.org/10.1149/2162-8777/acad27 (2022).
28. Abbas, M. N. & Amer, H. S. A solid-contact indium(III) sensor based on a thiosulfinate ionophore derived from omeprazole. *Bull. Korean Chem. Soc.* **34**, 1153–1159 (2013).
29. Magar, H. S., Abbas, M. N., Ali, M. B. & Ahmed, M. A. Picomolar-sensitive impedimetric sensor for salivary calcium analysis at POC based on SAM of Schiff base–modified gold electrode. *J. Solid State Electrochem.* **24**, 723–737 (2020).
30. Magar, H. S., Ghica, M. E., Abbas, M. N. & Brett, C. M. A. Highly sensitive choline oxidase enzyme inhibition biosensor for lead ions based on multiwalled carbon nanotube modified glassy carbon electrodes. *Electroanalysis* **29**, 1741–1748 (2017).
31. Magar, H. S., Hassan, R. Y. A. & Mulchandani, A. electrochemical impedance spectroscopy (EIS): Principles, construction, and biosensing applications. *Sensors* https://doi.org/10.3390/s21196578 (2021).
32. Magar, H. S., Magd, E.E.A.-E., Hassan, R. Y. A. & Fahim, A. M. Rapid impedimetric detection of cadmium ions using Nanocellulose/ligand/nanocomposite (CNT/Co_3O_4). *Microchem. J.* **182**, 107885 (2022).
33. Magar, H. S., Ghica, M. E., Abbas, M. N. & Brett, C. M. A. A novel sensitive amperometric choline biosensor based on multiwalled carbon nanotubes and gold nanoparticles. *Talanta* **167**, 462–469 (2017).
34. Elzwawy, A. *et al.* Exploring the structural and electrochemical sensing of wide bandgap calcium phosphate/CuxFe$_3$-xO_4 core-shell nanoceramics for H_2O_2 detection. *Mater. Today Commun.* **33**, 104574 (2022).
35. Abbas, M. & Amer, H. A novel solid-contact sensor for flow injection determination of verapamil in pharmaceutical formulations and urine. *Curr. Pharm. Anal.* **4**, 90–100 (2008).
36. Magar, H. S., Brahman, P. K. & Hassan, R. Y. A. Disposable impedimetric nano-immunochips for the early and rapid diagnosis of Vitamin-D deficiency. *Biosens. Bioelectron. X* **10**, 100124 (2022).
37. Kuz'Mina, L. G. *et al.* Influence of the anion nature on styryl dye crystal packing and feasibility of the direct and back [2 + 2] photocycloaddition reactions without single crystal degradation. *CrystEngComm* **16**, 5364–5378 (2014).
38. Momma, K. & Izumi, F. VESTA: A three-dimensional visualization system for electronic and structural analysis. *J. Appl. Crystallogr.* **41**, 653–658 (2008).
39. El-Menyawy, E. M., Zedan, I. T., Mansour, A. M. & Nawar, H. H. Thermal stability, AC electrical conductivity and dielectric properties of N-(5-{[antipyrinyl-hydrazono]-cyanomethyl}-[1,3,4]thiadiazol-2-yl)-benzamide. *J. Alloys Compd.* **611**, 50–56 (2014).
40. Mansour, A. M. Thermal microscopy (TM). *Int. J. Microstruct. Mater. Prop.* **15**, 215–228 (2020).
41. Ren, P., Fan, H. & Wang, X. Solid-state synthesis of Bi_2O_3/$BaTiO_3$ heterostructure: Preparation and photocatalytic degradation of methyl orange. *Appl. Phys. A Mater. Sci. Process.* **111**, 1139–1145 (2013).
42. Tariq, R. *et al.* Synthesis of carbon supported iron oxide nanochips and their composite with glutathione: A novel electrochemical sensitive material. *Surfaces and Interfaces* **34**, 102350 (2022).
43. Kousar, T. *et al.* Wet-chemical synthesis of nanostructured Ce-doped mixed metal ferrites for the effective removal of azo dyes from industrial discharges. *Ceram. Int.* **48**, 11858–11868 (2022).
44. Kousar, T. *et al.* Temperature controlled synthesis of Co-Ni mixed ferrite nanostructure for the mineralization of azo dye: A novel and facile approach. *J. Alloys Compd.* **923**, 166224 (2022).
45. Aamir, M. *et al.* Graphene oxide nanocomposite with Co and Fe doped LaCrO3 perovskite active under solar light irradiation for the enhanced degradation of crystal violet dye. *J. Mol. Liq.* **322**, 114895 (2021).
46. El Nahrawy, A. M., Hammad, A. B. A., Youssef, A. M., Mansour, A. M. & Othman, A. M. Thermal, dielectric and antimicrobial properties of polystyrene-assisted/ITO: Cu nanocomposites. *Appl. Phys. A* **125**, 46 (2019).
47. Mansour, A. M., Radaf, I. M. E., Hameed, T. A. & Sakr, G. B. Investigation of ag2hgi4 nanoparticles: Thermal phase transition and non-isothermal kinetic study. *UPB Sci Bull. Ser. B Chem. Mater. Sci.* **81**, 134–148 (2019).
48. Gioti, S. *et al.* Multitasking performance of Fe_3O_4/$BaTiO_3$/Epoxy resin hybrid nanocomposites. *Materials (Basel)* **15**, 1784 (2022).
49. Dang, N. V. *et al.* Structure of BaTi1− xFexO_3− δ multiferroics using X-ray analysis. *Chinese J. Phys.* **50**, 262 (2012).
50. El Nahrawy, A. M., AbouHammad, A. B. & Mansour, A. M. Structural investigation and optical properties of Fe, Al, Si, and Cu-ZnTiO3nanocrystals. *Phys. Scr.* **96**, 115801 (2021).
51. Ibrahim, R. S., Azab, A. A. & Mansour, A. M. Synthesis and structural, optical, and magnetic properties of Mn-doped CdS quantum dots prepared by chemical precipitation method. *J. Mater. Sci. Mater. Electron.* **32**, 19980–19990 (2021).
52. Mansour, A. M., AbouHammad, A. B., Bakr, A. M. & El Nahrawy, A. M. Silica Zinc Titanate Wide Bandgap semiconductor nanocrystallites: Synthesis and characterization. *SILICON* **14**, 11715–11729 (2022).
53. Abram, R. A., Childs, G. N. & Saunderson, P. A. Band gap narrowing due to many-body effects in silicon and gallium arsenide. *J. Phys. C Solid State Phys.* **17**, 6105–6125 (1984).
54. Tripathy, S. K. Refractive indices of semiconductors from energy gaps. *Opt. Mater. (Amst)* **46**, 240–246 (2015).
55. Pal, S., Kumar Tiwari, R., Chandra Gupta, D. & Singh Verma, A. Simplistic theoretical model for optoelectronic properties of compound semiconductors. *J. Mater. Phys. Chem.* **2**, 20–27 (2014).
56. Duffy, J. A. Ultraviolet transparency of glass: A chemical approach in terms of band theory, polarisability and electronegativity. *Phys. Chem. Glasses* **42**, 151–157 (2001).
57. Linus Pauling. *The nature of the chemical bond, an introduction to modern structural chemistry*. (Cornell University Press, 1960).
58. Mansour, A. M., Hemdan, B. A., Elzwawy, A., AbouHammad, A. B. & El Nahrawy, A. M. Ecofriendly synthesis and characterization of Ni_2+ codoped silica magnesium zirconium copper nanoceramics for wastewater treatment applications. *Sci. Rep.* **12**, 9855 (2022).
59. El Nahrawy, A. M., Mansour, A. M., Elzwawy, A., Abou Hammad, A. B. & Hemdan, B. A. Spectroscopic and magnetic properties of Co0.15Al0.25-xNi0.6+xFe_2O_4nanocomposites aided by silica for prohibiting pathogenic bacteria during sewage handling. *Environ. Nanotechnology, Monit. Manag.* **18**, 100672 (2022).
60. Kong, L. *et al.* Interconnected 1D Co_3O_4 nanowires on reduced graphene oxide for enzymeless H_2O_2 detection. *Nano Res.* **8**, 469–480 (2015).
61. Jiménez-Pérez, R., González-Rodríguez, J., González-Sánchez, M.-I., Gómez-Monedero, B. & Valero, E. Highly sensitive H_2O_2 sensor based on poly(azure A)-platinum nanoparticles deposited on activated screen printed carbon electrodes. *Sensors Actuators B Chem.* **298**, 126878 (2019).
62. Zhang, Y. *et al.* Highly sensitive graphene–pt nanocomposites amperometric biosensor and its application in living Cell H_2O_2 detection. *Anal. Chem.* **86**, 9459–9465 (2014).
63. Sun, Y., He, K., Zhang, Z., Zhou, A. & Duan, H. Real-time electrochemical detection of hydrogen peroxide secretion in live cells by Pt nanoparticles decorated graphene–carbon nanotube hybrid paper electrode. *Biosens. Bioelectron.* **68**, 358–364 (2015).
64. Barkaoui, S., Haddaoui, M., Dhaouadi, H., Raouafi, N. & Touati, F. Hydrothermal synthesis of urchin-like Co_3O_4 nanostructures and their electrochemical sensing performance of H_2O_2. *J. Solid State Chem.* **228**, 226–231 (2015).

Author contributions

A.B.A.H.: Analyzed and interpreted the data; Contributed reagents, materials, analysis tools, or data; Wrote the paper, and submitted the paper to the journal. H.S.M. and R.Y.A.H.: Analyzed and interpreted the electrochemical data; materials, analysis tools, or data; Wrote the paper. A.M.M.: Analyzed and interpreted the data; Contributed reagents, materials, analysis tools, or data; Wrote the paper. A.M.E.N.: Conceived and designed the

experiments; Analyzed and interpreted the data; Contributed reagents, materials, analysis tools, or data; Wrote the paper. All author(s) read and approved the final manuscript.

Funding

Open access funding provided by The Science, Technology & Innovation Funding Authority (STDF) in cooperation with The Egyptian Knowledge Bank (EKB).

Competing interests

The authors declare no competing interests.

Additional information

Supplementary Information The online version contains supplementary material available at https://doi.org/10.1038/s41598-023-36076-6.

Correspondence and requests for materials should be addressed to A.M.E.N.

Reprints and permissions information is available at www.nature.com/reprints.

Publisher's note Springer Nature remains neutral with regard to jurisdictional claims in published maps and institutional affiliations.